Topics in Catalysis
https://doi.org/10.1007/s11244-026-02281-6

ORIGINAL PAPER

NHC based Pd-PEPPSI complexes: synthesis, computational studies and application for Suzuki and direct arylation reactions

Nour-Elhouda Belazghem[1] · Öznur Doğan Ulu[2,3] · Sümeyya Serin[3] · İlkay Yıldırım[4] · Khaled Sekkoum[1] · Namık Özdemir[5] · İsmail Özdemir[2,6,7]

Accepted: 3 March 2026
© The Author(s) 2026

Abstract
A series of novel air- and moisture-resistant NHC-based pyridine containing palladium PEPPSI-type Pd(II) complexes (**2a-e**) were synthesized and characterized. The structures of all synthesized complexes were determined by various spectroscopic techniques. In addition, the structure of **2b** was elucidated by single X-ray crystallography. The structural and electronic properties of **2a-e** were further investigated using DFT calculations, which provided valuable insights into thermodynamic parameters, frontier molecular orbitals, and natural bond orbital interactions. The experimental and theoretical data showed strong agreement, confirming the robustness of the applied methodology. The complexes were successfully employed in the Suzuki cross-coupling of phenylboronic acid with aryl chlorides using green solvents. Also, the complexes were tested for direct arylation reactions and obtained mild to good yields.

Keywords Palladium · PEPPSI · DFT · Catalytic activity

1 Introduction

Transition metal-catalyzed reactions for the formation of carbon-carbon and carbon-heteroatom bonds constitute a crucial component of modern organic synthesis [1–3]. In this context, palladium-based catalysts, in particular, are among the most preferred systems for many reactions such as arylation [4], amination [5], and C-C coupling reactions [3, 6, 7], thanks to their high efficiency, wide substrate range, and good functional group tolerance [8]. Palladium-catalyzed protocols, such as the Suzuki–Miyaura reaction and direct arylation reactions, allow for the synthesis of complex molecules in fewer steps and under more environmentally sustainable conditions and are widely used in many fields, including pharmaceutical chemistry, materials science, and agrochemicals [9–11].

One of the key factors directly affecting catalyst performance in such reactions is the ligand environment surrounding the metal center. In recent years, *N*-heterocyclic carbenes (NHCs) have gained prominence as alternatives to phosphines in Pd complexes due to their strong σ-donor properties, broad electronic tunability, and high thermal and chemical stability [12–16]. NHC ligands, thanks to their ability to stabilize Pd(II) and Pd(0) species, can effectively control the formation and transformation of active species throughout the catalytic cycle [13, 15]. In this context, the design of NHC-based Pd complexes plays a decisive role in both the selectivity and rate of catalytic processes.

Pd-PEPPSI (Pyridine-Enhanced Precatalyst Preparation Stabilization and Initiation) complexes, reported by Organ in 2006, are particularly notable for their ease of preparation,

✉ İsmail Özdemir
ismail.ozdemir@inonu.edu.tr

1 Bioactive Molecules and Chiral Separation Laboratory, Faculty of Exact Sciences, Tahri Mohammed University, 08000 Bechar, Algeria

2 Catalysis Research and Application Center, İnönü University, Malatya 44280, Türkiye

3 İnönü University, Scientific and Technological Research Center, Malatya 44280, Türkiye

4 Vocational School, Department of Radiotherapy, Biruni University, 34015 İstanbul, Türkiye

5 Faculty of Science, Department of Physics, Ondokuz Mayıs University, Samsun 55139, Türkiye

6 Faculty of Arts and Sciences, Department of Chemistry, İnönü University, Malatya 44280, Türkiye

7 Drug Application and Research Center, İnönü University, Malatya 44280, Türkiye

Published online: 17 March 2026

high stability against air and moisture, and rapid activation properties [17]. The pyridine auxiliary ligand in these complexes directly influences the solubility and activation behavior of the precatalyst, significantly impacting catalytic performance. Therefore, structural modifications to the ligand architecture of PEPPSI complexes can have profound effects on the efficiency and selectivity of the catalytic system [18–20].

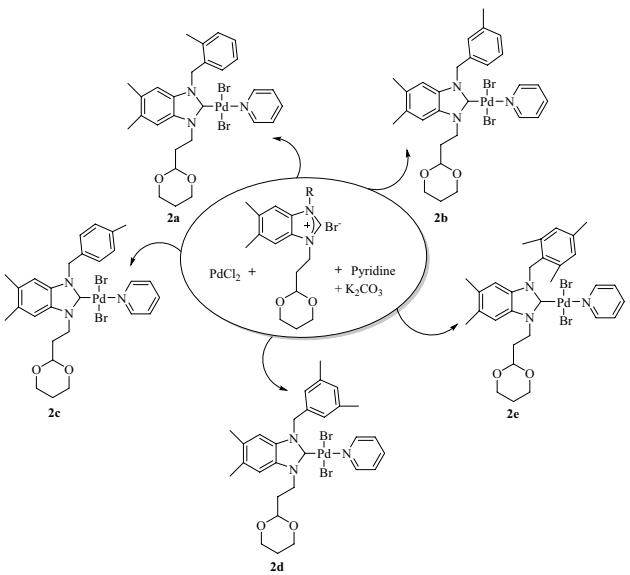
In this study, Pd-PEPPSI complexes containing NHC ligands with various structural properties were synthesized, and their structural and electronic properties were investigated in detail using both experimental methods (Nuclear Magnetic Resonance (NMR), X-ray crystallography, etc.) and density functional theory (DFT)-based computational approaches. The catalytic activities of the resulting complexes in Suzuki–Miyaura cross-coupling and direct C–H arylation reactions were evaluated, and the effects of ligand structure on catalytic efficiency, conversion time, and selectivity were comparatively analyzed. In this context, the study provides important structural-catalytic relationships that can contribute to the design of sustainable and highly efficient catalysts.

2 Experimental

2.1 Chemicals and methods

The synthesis of all compounds was executed through the utilization of the Schlenk technique in an inert atmosphere. It is imperative to note that no purification or drying process was performed on the solvents and reagents utilized in the experimental setting. The Suzuki reaction was carried out in air using a green solvent system composed of isopropanol (*i*-PrOH)-H_2O. While some of the reagents utilized in these reactions were synthesized in our laboratory, others, including pyridine, *n*-pentane, dichloromethane (DCM) and *i*-PrOH, were procured from commercial sources.

NMR spectra were taken on a Bruker Ultra Shield 400 MHz spectrometer using deuterated chloroform ($CDCl_3$) as solvent and tetramethyl silane (TMS) as internal standard. Fourier Transform Infrared Spectroscopy (FT-IR) spectra were taken in the Perkin Elmer Spectrum 100 spectrometer in the range of 650–4000 cm^{-1}. Melting points were determined with an Electrothermal melting point detector. Gas Chromatography-Mass Spectrometry (GC-MS) analyses were carried with the GC system of Agilent Technologies 6890 N Network system gas chromatography equipped with an Agilent Technologies 5973 inert Mass Selective Detector.



Scheme 1 The general synthesis of Pd-PEPPSI complexes

2.2 The synthesis of NHC-based Pd-PEPPSI complexes (2a-e)

NHC based Pd-PEPPSI complexes (**2a-e**) were obtained through a reaction involving 1 mmol of benzimidazolium salt, 1 mmol of palladium(II) chloride ($PdCl_2$), 5 mmol of potassium carbonate (K_2CO_3), and a substantial quantity of potassium bromide (KBr) in pyridine at 80 °C for a duration of 5 h. Subsequent to the completion of the reaction, the residue was subjected to vacuum removal of pyridine, followed by the addition of dichloromethane. The resulting suspension was passed over silica gel, and the solvent was removed under vacuum. The desired Pd-PEPPSI complexes (**2a-e**) were crystallized in a mixture of DCM and pentane, and were isolated with satisfactory yields. The general synthesis of Pd-PEPPSI complexes (**2a-e**) was shown in Scheme 1.

2.2.1 Dibromo [1-(2-methylbenzyl)-5,6-dimethyl-3-(2-(1,3-dioxane-2-yl)ethyl) benzimidazol-2-ylidene]pyridine palladium (II), *2a*

Yield: Yellow solid, 74%, m.p.:221–222 °C, FT-IR $\nu_{(C-N)}$:1417 cm^{-1}, ^1H NMR (400 MHz, $CDCl_3$): δ 1.35 and 2.13 (m, 2 H, NCH_2CH_2-1,3-dioxane-5-CH_2); 2.20 and 2.34 (s, 6 H, C_6H_2-CH_3-5,6); 2.49 (s, 3 H, (2-CH_3) C_6H_4-CH_2); 2.57 (m, 2 H, NCH_2CH_2-1,3-dioxane); 3.80 and 4.14 (m, 4 H, NCH_2CH_2-1,3-dioxane-4,6-CH_2); 4.78 (t, 1H, *J*=8 Hz, NCH_2CH_2-1,3-dioxane-2-C*H*); 4.96 (t, *J*=8 Hz, 2 H, NCH_2CH_2-1,3-dioxane); 6.01 (s, 2 H, (3-CH_3)C_6H_4-CH_2); 6.68–726 (m, 9 H, (2-CH_3)C_6H_4-CH_2, C_6H_4), 7.29–7.33 and 7.72–7.75 (m, 2 H, CH_{Py}); 8.99 (dd,, *J*=4 Hz, 2 H, C$H_{Py-ortho}$). ^{13}C NMR (100 MHz, $CDCl_3$): δ 19.8 ((2-CH_3)C_6H_5-CH_2); 20,2 (C_6H_2-CH_3-5,6); 25.8

(NCH_2CH_2-1,3-dioxane-5-*C*H_2), 34.5 (NCH_2CH_2-1,3-dioxane); 43.9 (N*C*H_2CH_2-1,3-dioxane); 50.5 ((2-CH_3)C_6H_5-*C*H_2), 66.8 (NCH_2CH_2-1,3-dioxane-4,6-*C*H_2); 99.5 (NCH_2CH_2-1,3-dioxane-2-*C*H); 111.0, 111.4, 124.4, 126.3, 127.8, 128.4, 130.3, 132.2, 133.2, 133.4, 135.5, 137.8 (Ar-*C*); 152.6 (*C*$H_{Py-ortho}$); 161.3 (Pd-$C_{carbene}$).

2.2.2 Dibromo [1-(3-methylbenzyl)-5,6-dimethyl-3-(2-(1,3-dioxane-2-yl)ethyl) benzimidazol-2-ylidene]pyridine palladium (II), *2b*

Yield: Yellow crystalline solid, 70%, m.p.:167–168 °C, FT-IR $\nu_{(C-N)}$:1405 cm^{-1}, ^{1}H NMR (400 MHz, $CDCl_3$): δ 1.36 and 2.13 (m, 2 H, NCH_2CH_2-1,3-dioxane-5-CH_2); 2.22 (s, 6 H, C_6H_2-CH_3-5,6); 2.32 (s, 3 H, (3-CH_3)C_6H_4-CH_2); 2.58 (m, 2 H, NCH_2CH_2-1,3-dioxane); 3.80 and 4.14 (m, 4 H, NCH_2CH_2-1,3-dioxane-4,6-CH_2); 4.78 (t, 1H, *J*=8 Hz, NCH_2CH_2-1,3-dioxane-2-C*H*); 4.97 (t, *J*=8 Hz, 2 H, NCH_2CH_2-1,3-dioxane); 6.03 (s, 2 H, (3-CH_3)C_6H_4-CH_2); 7.10–7.26 (m, 9 H, (3-CH_3)C_6H_4-CH_2, C_6H_4), 7.30–7.34 and 7.72–7.76 (m, 2 H, CH_{Py}); 9.03 (d,, *J*=4 Hz, 2 H, C$H_{Py-ortho}$). ^{13}C NMR (100 MHz, $CDCl_3$): δ 20.2 ((3-*C*H_3)C_6H_5-CH_2); 21.4 (C_6H_2-*C*H_3-5,6); 25.8 (NCH_2CH_2-1,3-dioxane-5-*C*H_2), 34.5 (NCH_2CH_2-1,3-dioxane); 43.8 (N*C*H_2CH_2-1,3-dioxane); 53.3 ((3-CH_3)C_6H_5-*C*H_2), 66.7 (NCH_2CH_2-1,3-dioxane-4,6-*C*H_2); 99.5 (NCH_2CH_2-1,3-dioxane-2-*C*H); 111.6, 124.5, 125.0, 128.5, 128.7, 132.1, 132.2, 133.1, 133.6, 135.1, 137.8, 138.5 (Ar-*C*); 152.6 (*C*$H_{Py-ortho}$); 161.0 (Pd-$C_{carbene}$).

2.2.3 Dibromo [1-(4-methylbenzyl)-5,6-dimethyl-3-(2-(1,3-dioxane-2-yl)ethyl) benzimidazol-2-ylidene]pyridine palladium (II), *2c*

Yield: Yellow solid, 73%, m.p.:196–197 °C, FT-IR $\nu_{(C-N)}$:1444 cm^{-1}, ^{1}H NMR (400 MHz, $CDCl_3$): δ 1.35 and 2.12 (m, 2 H, NCH_2CH_2-1,3-dioxane-5-CH_2); 2.21 (s, 3 H, (4-CH_3)C_6H_4-CH_2); 2.32 (s, 6 H, C_6H_2-CH_3-5,6); 2.57 (q,, *J*=8 Hz, 2 H, NCH_2CH_2-1,3-dioxane); 3.80 and 4.14 (m, 4 H, NCH_2CH_2-1,3-dioxane-4,6-CH_2); 4.78 (t, 1H, *J*=8 Hz, NCH_2CH_2-1,3-dioxane-2-C*H*); 4.97 (t, *J*=8 Hz, 2 H, NCH_2CH_2-1,3-dioxane); 6.05 (s, 2 H, (4-CH_3)C_6H_4-CH_2); 6.80–7.34 (m, 9 H, (4-CH_3)C_6H_4-CH_2, C_6H_4), 7.44–7.47 and 7.72–7.76 (m, 2 H, CH_{Py}); 9.03 (d,, *J*=4 Hz, 2 H, C$H_{Py-ortho}$). ^{13}C NMR (100 MHz, $CDCl_3$): δ 20.2 ((4-*C*H_3)C_6H_5-CH_2); 21.2 (C_6H_2-*C*H_3-5,6); 25.8 (NCH_2CH_2-1,3-dioxane-5-*C*H_2), 34.5 (NCH_2CH_2-1,3-dioxane); 43.8 (N*C*H_2CH_2-1,3-dioxane); 53.4 ((4-CH_3)C_6H_5-*C*H_2), 66.7 (NCH_2CH_2-1,3-dioxane-4,6-*C*H_2); 99.5 (NCH_2CH_2-1,3-dioxane-2-*C*H); 110.9, 111.7, 124.5, 127.9, 129.4, 132.0, 132.1, 132.9, 133.7, 137.6, 137.8 (Ar-*C*); 152.6 (*C*$H_{Py-ortho}$); 160.9 (Pd-$C_{carbene}$).

2.2.4 Dibromo [1-(3,5-dimethylbenzyl)-5,6-dimethyl-3-(2-(1,3-dioxane-2-yl)ethyl) benzimidazol-2-ylidene]pyridine palladium (II), *2d*

Yield: Yellow solid, 68%, m.p.:244–245 °C, FT-IR $\nu_{(C-N)}$:1405 cm^{-1}, ^{1}H NMR (400 MHz, $CDCl_3$): δ 1.38 and 2.17 (m, 2 H, NCH_2CH_2-1,3-dioxane-5-CH_2); 2.23 and 2.33 (s, 3 H, (3,5-CH_3)C_6H_4-CH_2); 2.29 (s, 6 H, C_6H_2-CH_3-5,6); 2.57 (q,, *J*=8 Hz, 2 H, NCH_2CH_2-1,3-dioxane); 3.80 and 4.14 (m, 4 H, NCH_2CH_2-1,3-dioxane-4,6-CH_2); 4.78 (t, 1H, *J*=4 Hz, NCH_2CH_2-1,3-dioxane-2-C*H*); 4.97 (t, *J*=8 Hz, 2 H, NCH_2CH_2-1,3-dioxane); 5.98 (s, 2 H, (3,5-CH_3)C_6H_4-CH_2); 6.86–6.93 and 7.20–7.29 (m, 9 H, (3,5-CH_3)C_6H_4-CH_2, C_6H_4), 7.31–7.34 and 7.72–7.76 (m, 2 H, CH_{Py}); 9.02 (d,, *J*=4 Hz, 2 H, C$H_{Py-ortho}$). ^{13}C NMR (100 MHz, $CDCl_3$): δ 20.2 ((3,5-*C*H_3)C_6H_5-CH_2); 21.3 (C_6H_2-*C*H_3-5,6); 25.8 (NCH_2CH_2-1,3-dioxane-5-*C*H_2), 34.6 (NCH_2CH_2-1,3-dioxane); 43.8 (N*C*H_2CH_2-1,3-dioxane); 53.2 ((3,5-CH_3)C_6H_5-*C*H_2), 66.7 (NCH_2CH_2-1,3-dioxane-4,6-*C*H_2); 99.5 (NCH_2CH_2-1,3-dioxane-2-*C*H); 110.9, 111.6, 124.5, 125.7, 129.6, 132.0, 132.1, 133.1, 133.6, 135.1, 137.8, 138.2 (Ar-*C*); 152.6 (*C*$H_{Py-ortho}$); 160.9 (Pd-$C_{carbene}$).

2.2.5 Dibromo [1-(2,4,6-trimethylbenzyl)-5,6-dimethyl-3-(2-(1,3-dioxane-2-yl)ethyl) benzimidazol-2-ylidene] pyridine palladium (II), *2e*

Yield: Yellow solid, 75%, m.p.:184–185 °C, FT-IR $\nu_{(C-N)}$:1406 cm^{-1}, ^{1}H NMR (400 MHz, $CDCl_3$): δ 1.31 and 2.07 (m, 2 H, NCH_2CH_2-1,3-dioxane-5-CH_2); 2.28 and 2.30 (s, 3 H, (2,4,6-CH_3)C_6H_4-CH_2); 2.35 (s, 6 H, C_6H_2-CH_3-5,6); 2.55 (q,, *J*=8 Hz, 2 H, NCH_2CH_2-1,3-dioxane); 3.77 and 3.94 (m, 4 H, NCH_2CH_2-1,3-dioxane-4,6-CH_2); 4.73 (t, 1H, *J*=4 Hz, NCH_2CH_2-1,3-dioxane-2-C*H*); 4.95 (t, *J*=8 Hz, 2 H, NCH_2CH_2-1,3-dioxane); 6.03 (s, 2 H, (2,4,6-CH_3)C_6H_4-CH_2); 6.92–7.03 and 7.19–7.26 (m, 9 H, (2,4,6-CH_3)C_6H_4-CH_2, C_6H_4), 7.31–7.43 and 7.74–7.79 (m, 2 H, CH_{Py}); 9.03 (t,, *J*=4 Hz, 2 H, C$H_{Py-ortho}$). ^{13}C NMR (100 MHz, $CDCl_3$): δ 20.3 ((2,4,6-*C*H_3)C_6H_5-CH_2); 20.9 (C_6H_2-*C*H_3-5,6); 25.8 (NCH_2CH_2-1,3-dioxane-5-*C*H_2), 34.6 (NCH_2CH_2-1,3-dioxane); 46.7 (N*C*H_2CH_2-1,3-dioxane); 50.5 ((2,4,6-CH_3)C_6H_5-*C*H_2), 66.7 (NCH_2CH_2-1,3-dioxane-4,6-*C*H_2); 99.6 (NCH_2CH_2-1,3-dioxane-2-*C*H); 110.7, 111.7, 112.8, 124.5, 125.0, 127.8, 129.4, 130.0, 131.7, 138.5 (Ar-*C*); 152.6 (*C*$H_{Py-ortho}$); 160.6 (Pd-$C_{carbene}$).

2.3 X-ray crystallography

Intensity data of **2b** were collected on a Bruker D8 QUEST diffractometer at 296(2) K using graphite-monochromated Mo Kα radiation by applying the φ and ω scan methods. Data collection was carried out using APEX2 [21] while cell

refinement and data reduction were applied using SAINT [21]. The structure was solved by a dual-space algorithm using SHELXT-2018 [22] and refined by means of the full-matrix least-squares calculations on F^2 using SHELXL-2019 [23]. All the H atoms were inserted in idealized positions and treated using a riding model, fixing the bond lengths at 0.98, 0.93, 0.97 and 0.96 Å for methine CH, aromatic CH, CH_2 and CH_3 atoms, respectively. The displacement parameters of the H atoms were fixed at $U_{iso}(H) = 1.2U_{eq}$ ($1.5U_{eq}$ for CH_3). Table 1 compiles information on crystal data, data collection, and structure refinement. Molecular graphic was generated utilizing OLEX2 [24].

2.4 Computational theory

All geometry optimizations and vibrational frequency analyses for compounds **2a–e** were conducted using the GAUSSIAN 16 software package [25]. The B3LYP hybrid exchange-correlation functional [26–28] was employed throughout, together with the 6-311 + + G(d, p) basis set for non-metal atoms (C, H, N, O, and Br), while the LANL2DZ effective core potential were used for the Pd center [29]. Molecular visualizations including optimized geometries, frontier molecular orbitals, and electrostatic potential surfaces were generated using GaussView 6 software [30]. The absence of imaginary vibrational frequencies confirmed that all structures correspond to local minima on the potential energy surface.

The thermodynamic parameters, including enthalpy (ΔH), entropy (S), Gibbs free energy (ΔG), and heat capacity at constant volume (Cv), were derived from vibrational frequency calculations using standard statistical thermodynamics [31–35]. The main contribution to these quantities arises from vibrational modes. Accordingly, the vibrational energy (Evib), vibrational entropy (Svib), and vibrational heat capacity (Cvvib) for compounds **2a–e** were calculated using Eqs. (1)–(5), based on the harmonic oscillator approximation. The following explanations refer to the terms given in the equations: $\Theta_{v,j} = hvj/k \rightarrow$vibrational temperature, $k\rightarrow$ Boltzmann constant, $h\rightarrow$ Planck constant, and $vj\rightarrow j^{th}$ fundamental frequency.

$$Q = Q_{trans.} \times Q_{rot.} \times Q_{vib.} Q_{elec.} \tag{1}$$

$$Q_{vib.} = \prod_{j=1}^{3N-6} \frac{e^{-\Theta_{\nu,j}/2T}}{\left(1 - e^{-\frac{\Theta_{\nu,j}}{T}}\right)} \tag{2}$$

$$E_{vib.} = Nk \sum_{j=1}^{3N-6} \left(\frac{\Theta_{\nu,j}}{2} + \frac{\Theta_{\nu,j} e^{-\Theta_{\nu,j}/T}}{\left(1 - e^{-\frac{\Theta_{\nu,j}}{T}}\right)} \right) \tag{3}$$

$$S_{vib.} = Nk \sum_{j=1}^{3N-6} \left[\frac{\Theta_{\nu,j}/T}{\left(e^{\Theta_{\nu,j}/T} - 1\right)} - ln\left(1 - e^{-\Theta_{\nu,j}/T}\right) \right] \tag{4}$$

$$Cv_{vib.} = Nk \sum_{j=1}^{3N-6} \left[\left(\frac{\Theta_{v,j}}{T}\right)^2 \frac{e^{\Theta_{\nu,j}/T}}{\left(e^{\Theta_{\nu,j}/T} - 1\right)^2} \right] \tag{5}$$

FMO (Frontier Molecular Orbital) theory computations were carried out to gain insights into the reactive sites and chemical reactivity behavior of compounds **2a–e.** Ionization energy (I) ($I = -E_{HOMO}$) and electron affinity (A) ($A = -E_{LUMO}$) values were derived based on Koopmans' theorem [36], relating them to the energies of the HOMO and LUMO orbitals. Furthermore, several quantum chemical reactivity descriptors including chemical hardness (η), chemical potential (μ), electronegativity (χ), electrophilicity index (ω), maximum charge transfer capacity (ΔN_{max}), back-donation energy ($\Delta E_{back-donation}$), electron-accepting power (ω^+), and electron-donating power (ω^-) were calculated

Table 1 Crystal data and structure refinement parameters for **2b**

CCDC depository	2,482,468
Color/shape	Yellow/block
Chemical formula	$[PdBr_2(C_{23}H_{28}N_2O_2)(C_5H_5N)]$
Formula weight	709.79
Temperature (K)	296(2)
Wavelength (Å)	0.71073 Mo Kα
Crystal system	Monoclinic
Space group	$P2_1/n$ (No. 14)
Unit cell parameters	
a, b, c (Å)	13.384(3), 14.613(4), 14.474(4)
α, β, γ (°)	90, 92.055(8), 90
Volume (Å^3)	2829.0(13)
Z	4
$D_{calc.}$ (g/cm^3)	1.667
μ (mm^{-1})	3.510
Absorption correction	Multi-scan
$T_{min.}$, $T_{max.}$	0.6542, 0.7454
F_{000}	1416
Crystal size (mm^3)	0.04 × 0.03 × 0.01
Diffractometer	Bruker D8 QUEST
Measurement method	φ and ω scan
Index ranges	$-16 \le h \le 15$, $-18 \le k \le 18$, $-18 \le l \le 18$
θ range for data collection (°)	$1.981 \le \theta \le 26.759$
Reflections collected	72,577
Independent/observed reflections	5972/2993
$R_{int.}$	0.1198
Refinement method	Full-matrix least-squares on F^2
Data/restraints/parameters	5972/0/328
Goodness-of-fit on F^2	1.025
Final R indices [$I > 2\sigma(I)$]	$R_1 = 0.0523$, $wR_2 = 0.0933$
R indices (all data)	$R_1 = 0.1458$, $wR_2 = 0.1198$
$\Delta\rho_{max.}$, $\Delta\rho_{min.}$ (e/Å^3)	0.52, −0.99

using Eqs. (6, 7, 8, 9, 10, 11, 12, 13) as reported in the literature [37–43].

$$?= -\frac{I + A}{2} \tag{6}$$

$$? = \frac{I - A}{2} \tag{7}$$

$$\chi = \frac{I + A}{2} \tag{8}$$

$$\omega = \frac{\mu^2}{2?} \tag{9}$$

$$\omega^{+} \approx (I + 3A)^2/(16(I - A)) \tag{10}$$

$$\omega^{-} \approx (3I + A)^2/(16(I - A)) \tag{11}$$

$$\Delta N_{max} = \frac{I + A}{2(I - A)} \tag{12}$$

$$\Delta\epsilon_{back-donation} = -\frac{\eta}{4} \tag{13}$$

Within the framework of the employed theoretical approach, Natural Bond Orbital (NBO) analysis was conducted for compounds **2a–e** based on second-order perturbation theory applied to the Fock matrix elements [44, 45]. This analysis enabled the evaluation of intramolecular donor–acceptor interactions and the corresponding stabilization energies. These energies were determined using Eq. (14), which involves the following parameters: $E^{(2)}$ denotes the stabilization energy; qi corresponds to the occupancy of the donor orbital; Fi_j represents the off-diagonal element of the Fock matrix; εi and ε_j are the diagonal elements referring to the energies of the donor and acceptor orbitals, respectively.

$$E^{(2)} = \Delta E_{ij} = qi\left[\frac{(Fij)^2}{(\epsilon j - \epsilon i)}\right] \tag{14}$$

2.5 General procedure for the Suzuki reaction catalyzed by Pd-PEPPSI complexes

The Pd-PEPPSI complex (0.25% mol), base (1 mmol), aryl halide (1 mmol), and phenylboronic acid (1.2 mmol) were placed into a 10-ml tube under air. Subsequently, a 1:3 mixture of *i*-PrOH and water was added to the tube. The mixture was subjected to heating at a temperature of 60 °C for a duration of three hours. The mixture was extracted with dichloromethane. The organic phase was then subjected to drying over magnesium sulfate ($MgSO_4$), followed by filtration through short silica to eliminate palladium residue. The yields were calculated by taking into account the conversions of aryl chlorides to products.

2.6 General procedure for the direct arylation of heteroaromatics with aryl bromides

The following reagents were dissolved in 2 mL of N, N-dimethyl acetamide (DMAc) in a Schlenk tube under argon atmosphere, as previously described in the literature [46]: a heteroarene (2.0 mmol), an aryl bromide (1.0 mmol), potassium acetate (KOAc) (1.0 mmol), and Pd-PEPPSI complexes (**2a-e**) (1 mol %). Subsequent to stirring at 120 °C for 2 h, the reaction mixture was cooled to room temperature and the solvent was removed under vacuum. The crude products were subsequently purified by column chromatography (silica gel 60–120 mesh) with diethyl ether/n-hexane (1:5). The purity of the compounds was verified through gas chromatography (GC). The conversions were calculated by taking into account the conversions of aryl bromides to products.

3 Results and discussion

3.1 Synthesis and characterization of Pd-PEPPSI complexes (2a-e)

The molecular design of the palladium complexes was meticulously developed by taking into account the steric and electronic properties of the R substituents on the NHC ligands. Pd complexes (**2a–e**) were synthesized as illustrated in Scheme 1, via the reaction of the corresponding NHC precursors with $PdCl_2$, K_2CO_3, and KBr in pyridine (5 mL), affording the Pd-PEPPSI complexes. These complexes were isolated as yellow solids in high yields and demonstrated excellent stability toward air and moisture.

The structural characterization of the Pd-PEPPSI complexes was performed using FT-IR spectroscopy, as well as proton (^{1}H) and carbon-13 (^{13}C) NMR spectroscopy. In addition, the structure of the complex **2b** was elucidated by single crystal X-ray diffraction analysis. In the FT-IR spectra, the characteristic stretching vibrations of the (CN) groups were observed in the range of 1405–1417 cm^{-1}. All NMR spectra were recorded in $CDCl_3$. In the ^{1}H NMR spectra, the ortho protons of the coordinated pyridine ligands appeared at 8.99, 9.03, 9.03, 9.02 and 9.03 ppm for complexes **2a–e**, respectively. The ^{13}C NMR spectra revealed downfield-shifted signals corresponding to the carbene carbon atoms (NCN), located at 161.3, 161.0, 160.9, 160.9, and 160.6 ppm, respectively. The melting points, yields, and ^{13}C

Table 2 General information about Pd-PEPPSI complexes

Compound	M-$C_{carbene}$	Yield (%)	Melting point
2a	161.33	74	221-222
2b	161.03	70	167-168
2c	160.89	73	196-197
2d	160.94	68	244-245
2e	160.58	75	184-185

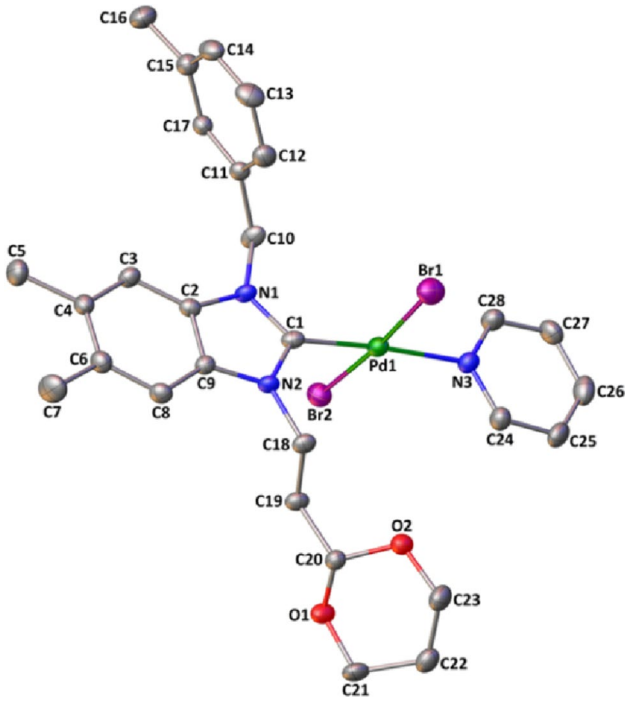


Fig. 1 Molecular structure of **2b** showing the atom-labelling scheme. Displacement ellipsoids are drawn at the 20% probability level and H atoms are omitted for clarity

Table 3 Selected geometric parameters for **2b**

Bond lengths (Å)			
Pd1—Br1	2.4314(10)	N1—C1	1.346(6)
Pd1—Br2	2.4243(9)	N1—C2	1.391(6)
Pd1—N3	2.087(4)	N2—C1	1.354(6)
Pd1—C1	1.945(5)	N2—C9	1.401(6)
Bond angles (°)			
Br1—Pd1—Br2	175.33(3)	Br2—Pd1—C1	87.83(14)
Br1—Pd1—N3	92.21(12)	N3—Pd1—C1	175.7(2)
Br2—Pd1—N3	90.71(11	N1—C1—N2	106.7(4)
Br1—Pd1—C1	89.51(14)		

NMR chemical shift values of the Pd complexes are presented in Table 2.

The absence of the characteristic resonances of the benzimidazolium salts in the NMR spectra of the complexes provides strong evidence for the successful formation of the Pd-PEPPSI framework. All data are compatible with literatüre [51]. Comprehensive spectral data are available in the Supporting Information (Fig. S1-S10).

3.2 Description of the structure

The molecular structure of **2b** with the atom-numbering scheme is shown in Fig. 1, while selected bond lengths and angles are listed in Table 3.

The complex is composed of a 1-[2-(1,3-dioxan-2-yl) ethyl]-5,6-dimethyl-3-(3-methylbenzyl)-2,3-dihydro-1*H*-benzo[*d*]imidazole ligand with a Pd^{II} metal center, a pyridine ligand and two bromo ligands in a *trans* configuration. The *cis* angles varying from 87.83(14) to 92.21(12)° and the *trans* angles changing from 175.33(3) to 175.7(2)° deviate from their expected values of 90 and 180°. For quantitative evaluation of the extent of distortion around the metal center, the four-coordinate structural indexes τ_4 [47], τ_4' [48] and τ_δ [49],

$$\tau_4 = \frac{360° - (\alpha + \beta)}{360° - 2\theta} \tau_4' = \frac{\beta - \alpha}{360° - \theta} + \frac{180° - \beta}{180° - \theta} \tau_\delta = \frac{360° - (\alpha + \beta)}{360° - 2\theta} \times \frac{\alpha}{\beta}$$

where α and β ($\beta > \alpha$) are the two greatest valence angles and θ is the ideal tetrahedral angle (109.5°), are employed. The τ_4, τ_4' and τ_δ values for ideal square-planar and tetrahedral coordination spheres are 0 and 1, respectively. All the τ_4, τ_4' and τ_δ values are 0.06, showing a slightly distorted square-planar structure. In the square-planar environment, the Pd atom is lying −0.0042(4) Å out the coordination plane defined by atoms Br1, Br2, N3 and C1.

The Pd—C_{NHC} bond distance [1.945(5) Å] is smaller than the sum of the individual covalent radii of the palladium and carbon atoms (2.12 Å), while the Pd—$N_{pyridine}$ bond distance [2.087(4) Å] is close to the sum of the individual covalent radii of the palladium and nitrogen atoms (2.10 Å) [50]. These values are in good agreement with those found in precedent Pd-NHC-Pyridine-Br_2 complexes [51–59]. In the imidazole ring, the N1—C1 and N2—C1 bonds are nearly equal [1.346(6) and 1.354(6) Å] and the N—C—N ring angle at the carbene center is 106.7(4)°. The carbene ring is oriented perpendiculary to the $PdCNBr_2$ coordination plane with a dihedral angle of 81.13(14)°. The dioxane ring adopts the usual chair conformation and the puckering parameters [60] are $Q = 0.541(6)$ Å, $q_2 = 0.054(6)$ Å, $q_3 = -0.539(6)$ Å, $\theta = 174.6(6)°$ and $\varphi_2 = 244(6)°$ for the atom sequence C20/O1/C21/C22/C23/O2.

3.3 Molecular structure and physicochemical properties

The computationally optimized structural parameters of **2a-e** were obtained using the B3LYP functional combined with the 6-311++G(d, p)/LANL2DZ basis set, and compared with experimental X-ray crystallography data. Table S1, which presents a comparative summary of the optimized

and experimental structural data, is included in the supplementary material. Also, Fig. 2 represents the optimized structures of **2a–e** complexes. The calculated Pd–Br bond lengths (2.515–2.520 Å) were found to be approximately 0.09 Å longer than the experimental values (2.4314/2.4243 Å). This systematic deviation may be attributed to the known limitations of the employed DFT method in modeling halogen-metal bonds or insufficient inclusion of relativistic effects. Similarly, the Pd1–N3 bond length was overestimated by about 0.087 Å relative to the experimental value of 2.087 Å. In contrast, the Pd1–C1 bond length was predicted at 1.983–1.985 Å, showing good agreement with the experimental value of 1.945 Å. The C–N bond lengths within the benzimidazole ligand framework matched the experimental data closely, with deviations typically within ±0.01 Å, indicating the computational method accurately describes the covalent bonding in the ligand backbone. Analysis of bond angles around the Pd center showed values close to an ideal square planar geometry. The Br1–Pd1–Br2 angle was near-linear both experimentally (175.33°) and computationally (174.80-175.08°), indicating minimal distortion along this coordination axis. Minor deviations (~1–2°) observed in Br–Pd–N3 and Br–Pd1–C1 angles could be due to steric effects or crystal packing forces. The most notable difference was observed in the N3–Pd1–C1 angle, which was nearly perfectly linear in the calculations (179.1-179.7°) but measured at 175.7° experimentally. This discrepancy may arise from weak intermolecular interactions in the crystal lattice or solid-state effects that are not accounted for in gas-phase optimizations. Overall, DFT optimizations performed at the B3LYP/6-311++G(d, p)/LANL2DZ level yield structural parameters largely consistent with experimental data. The ligand framework bond lengths and angles are well reproduced, while minor discrepancies in Pd-centered coordination bonds highlight the limitations inherent in the computational approach. Overall, the complex's geometry shows good agreement between theoretical and experimental results. Furtermore, the structural and electronic features obtained from X-ray diffraction and DFT calculations provide important insight into the observed catalytic behavior of the Pd–PEPPSI complexes. The short Pd–Ccarbene bond distances and the nearly linear N–Pd–C arrangement indicate strong σ-donation from the NHC ligand to the Pd center, which enhances the electron density on palladium. This electronic enrichment is crucial for facilitating the oxidative addition step of aryl halides, generally considered the rate-determining step in both Suzuki–Miyaura and direct arylation reactions.

Furthermore, thermodynamic properties and physical parameters of compounds **2a-e** were calculated, and the resulting data are compiled and presented in Table 4. The dipole moment (DM) values range from 2.13 to 2.51 Debye, indicating moderate polarity across all structures. The slight variation in DM suggests subtle changes in the overall charge distribution or molecular geometry, with complex **2c** showing the highest polarity (2.51 D) and **2e** the lowest (2.13 D). The total energy (ΔE), enthalpy (ΔH), and Gibbs free energy (ΔG) values show a clear trend of increasing stability from **2a** to **2e**, with **2e** being the most stable structure.The energy difference between **2a** and **2e** is substantial (~78.6 a.u. in ΔE), which suggests significant structural differences that lead to enhanced stabilization. These findings indicate that the introduction of the 2,4,6-trimethylbenzyl substituent contributes substantially to the stabilization of the complex, as reflected in the markedly lower Gibbs free energy of complex **2e**. On the other hand, the heat capacity (Cv) and entropy (S) also increase from **2a** to **2e**, with Cv rising from 135.883 to 147.912 cal/molK and

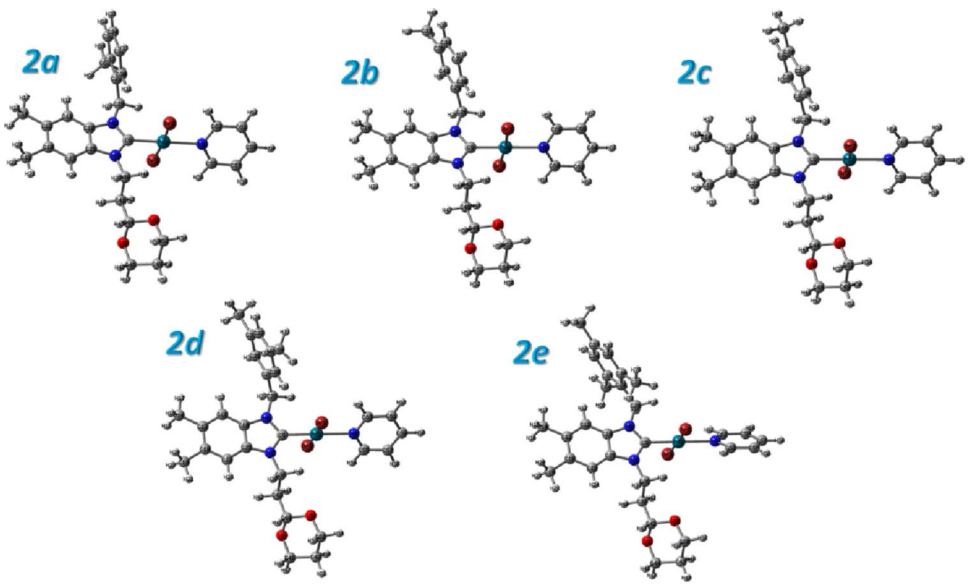


Fig. 2 The optimized structures of **2a-e**

Table 4 Thermodynamic and physicochemical parameter predictions for **2a-e**

	2a	2b	2c	2d	2e
DM (Debye)	2.45	2.37	2.51	2.46	2.13
ΔE (a.u.)	-6676.552488	-6676.555442	-6676.555738	-6715.856270	-6755.147727
ΔH (kJ/mol)	-17529189.9	-17529197.0	-17529197.8	-17632376.4	-17735532.3
ΔG (kJ/mol)	-17529493.2	-17529502.7	-17529503.7	-17632693.7	-17735856.1
$\Delta E_{thermal}$ (kcal/mol)	376.349	376.307	376.272	394.500	412.966
$\Delta E_{vib.}$ (kcal/mol)	374.572	374.530	374.495	392.723	411.189
Cv (cal/molK)	135.883	135.957	135.979	142.106	147.912
$Cv_{vib.}$ (cal/molK)	129.922	129.996	130.017	136.144	141.950
S (cal/molK)	243.165	245.046	245.225	254.378	259.608
$S_{vib.}$ (cal/molK)	159.235	161.031	161.202	170.186	175.257
α (a.u.)	451.91	454.32	454.79	467.19	478.80

S from 243.165 to 259.608 cal/molK. The enhancement of vibrational contributions to both heat capacity and entropy supports the hypothesis of augmented internal degrees of freedom in lower-energy structures. The polarizability (α) values, ranging from 451.91 to 478.80 a.u., exhibit a gradual increase across the series, which may reflect an enlargement of the molecular volume or an enhanced polarizability of the electron cloud. The higher polarizability observed in the more thermodynamically stable structures could be attributed to increased electronic delocalization or a more extended molecular framework.

3.4 FT-IR spectral analysis

This section presents a comprehensive overview of the theoretical and experimental FT-IR vibrational parameters of the newly synthesized Pd-NHC complexes **2a–e**, summarized in Table S3. The experimental FT-IR spectra are provided in Figures S12–S16. Harmonic vibrational wavenumbers were calculated at the B3LYP/6-311 + + G(d, p) level of theory and subsequently scaled to account for anharmonicity and basis set effects, using the literature-recommended factors of 0.958 for frequencies below 1700 cm^{-1} and 0.983 for frequencies above 1700 cm^{-1} [61]. Aromatic C-H stretching vibrations were predicted between 3127 and 3157 cm^{-1}, while aliphatic CH_2 and CH_3 stretching modes computed in the 2838–3086 cm^{-1} range, in good agreement with observed values (2845–3067 cm^{-1}). The C = C stretching vibrations of the benzimidazole and pyridine rings were detected at 1518–1603 cm^{-1}, consistent with calculated values of 1544–1594 cm^{-1} as pure modes. Characteristic C-O stretching vibrations associated with the 1,3-dioxane moieties appeared at 887–1243 cm^{-1}, closely matching DFT predictions (891–1243 cm^{-1}). The diagnostic νCN bands of the Pd-NHC complexes **2a-e** appear at 1095–1444 cm^{-1} compared to experimental values of 1092–1447 cm^{-1}, corresponding to deviations of approximately 1–7 cm^{-1}. These deviations are fully consistent with the expected performance of B3LYP calculations and can be attributed to the differences between gas-phase theoretical calculations and the ATR solid-state measurements. In addition to the stretching vibrations, characteristic ring breathing modes of the benzimidazole and pyridine fragments were computed in the 980–1197 cm^{-1} region. These modes, which involve symmetric in-plane deformation of the heteroaromatic rings, are sensitive to both metal coordination and substitution at the benzyl position [62, 63]. The ring breathing modes of the 1,3-dioxane moiety are clearly observed around 791–817 cm^{-1} in both experimental and theoretical spectra. These vibrations originate mainly from the symmetric deformation of the dioxane ring coupled with C–O stretching motions [64]. Out-of-plane bending (opb) vibrations of aromatic C-H and NCN groups were observed in the 671–968 cm^{-1} region, showing shifts that depended on the substitution pattern of the benzyl groups.

Table 5 The computed quantum chemical reactivity indices of **2a-e**

	2a	2b	2c	2d	2e
E_{HOMO}	-5.876	-5.876	-5.876	-5.872	-5.864
E_{LUMO}	-1.891	-1.887	-1.887	-1.884	-1.872
ΔE	3.985	3.989	3.989	3.988	3.992
η	1.993	1.995	1.995	1.994	1.996
μ	-3.884	-3.882	-3.882	-3.878	-3.868
χ	3.884	3.882	3.882	3.878	3.868
ω	3.785	3.777	3.777	3.771	3.748
ω^+	2.092	2.085	2.085	2.081	2.063
ω^-	5.975	5.967	5.967	5.959	5.931
ΔN_{max}	1.949	1.946	1.946	1.945	1.938
ΔE_{back}	-0.498	-0.499	-0.499	-0.499	-0.499

3.5 FMO & MEP analyses

The FMO energies (E_{HOMO} and E_{LUMO}) and related quantum chemical reactivity descriptors were calculated for all Pd complexes (**2a-e**). The data, summarized in Table 5, provide insight into the electronic characteristics and chemical reactivity of the complexes. The HOMO energies range from −5.876 eV to -5.864 eV, while the LUMO energies vary from −1.891 eV to -1.872 eV. Consequently, the HOMO–LUMO energy gap (ΔE) is relatively consistent across all structures, lying between 3.985 eV and 3.992 eV. A narrow

energy gap is typically associated with higher electronic polarizability and reactivity. However, in this case, the variation is minimal, indicating similar chemical hardness (η) among the complexes. The chemical hardness values were determined to range from 1.993 to 1.996 eV. The electronegativity (χ) values, ranging from 3.868 to 3.884 eV, suggest only slight variations among the **2a-e**, indicating that their tendencies for electron donation and acceptance are largely comparable. The electrophilicity index (ω) exhibits a slight decline from 3.785 eV for **2a** to 3.748 eV for **2e**, indicating a marginal reduction in electrophilic character in the more stable complexes. Likewise, the maximum charge transfer capacity (ΔNmax) shows a similar decreasing trend, from 1.949 to 1.938, further supporting the notion that complex **2e** is more electronically saturated and thermodynamically favored. The back-donation energy (ΔE_{back}) remains nearly constant at approximately − 0.499 eV across all structures, indicating that the extent of back-donation is not significantly influenced by structural variations among the complexes. Overall, the data indicate that the electronic properties of the complexes are largely comparable; however, complex **2e** demonstrates a more stable and less reactive nature, as evidenced by its lower electrophilicity and reduced electron-accepting capacity. These observations, consistent with the thermodynamic parameters and polarizability analyses, reinforce the conclusion that **2e** represents the most thermodynamically favorable structure among the complexes.

Furthermore, the HOMO–LUMO orbital distributions of five structurally related Pd-NHC complexes (**2a–e**) were investigated to evaluate the electronic effects of different methyl substitution patterns on the benzyl group of the NHC ligand. Figure 3 exhibits the 3D electron density distributions on the HOMOs and LUMOs of **2a-e**. The HOMO orbitals in all complexes were predominantly localized on the Pd (II) center and bromide ligands, remaining largely unaffected by the substituent variations. It should be noted that, although the LUMOs exhibit a predominantly metal-centered character similar to the HOMOs, their electron density displays a distinctly different spatial symmetry that varies depending on the nature and position of the substituents. Figure 3 also presents the molecular electrostatic potential (MEP) surface maps of the synthesized complexes. In MEP analysis, color gradients are used to represent the distribution of electrostatic potential on the molecular surface, facilitating the identification of nucleophilic and electrophilic regions [65, 66]. Within the MEP surface maps, the red color denotes regions with a high negative electrostatic potential, typically associated with nucleophilic character, while the blue color signifies areas of positive potential, corresponding to electrophilic character. MEP maps for complexes **2a-e** reveal that the negative potential is primarily localized around the Pd center and bromide ligands, reflecting the electron-rich nature of these regions. Light blue regions primarily localize to the aliphatic side chains and peripheral zones of the ligand scaffold.

3.6 NBO analysis

In contemporary research, Natural Bond Orbital (NBO) calculations are extensively employed across various molecular systems to elucidate phenomena such as charge transfer, electronic transitions, and potential donor-acceptor interactions. In this study, NBO analyses of the investigated **2a-e** complexes were performed consistently at the same level of theory. A comprehensive summary of the significant resonance interactions is presented in Table S2. The atomic numbering employed in this section is based on the DFT-optimized structure presented in Fig. 2. The NBO results provide detailed insights into the metal–ligand bonding and

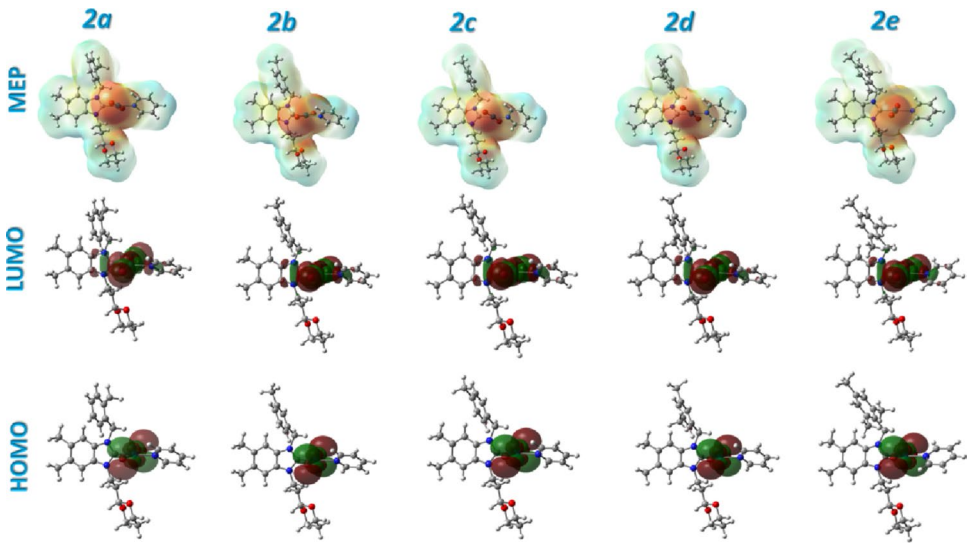


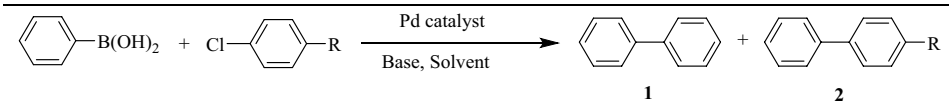
Fig. 3 HOMO-LUMO and MEP diagrams of **2a-e**

electronic delocalization within the Pd (II) complexes. Notably, the interactions from the σ(Pd1–C9) bonding orbital to the σ*(Pd1–Br) antibonding orbitals exhibit moderate stabilization energies ranging from approximately 14 to 20 kcal/mol across all complexes, indicating a robust bonding interaction between the palladium center and both the carbene and bromide ligands. Significant π → π* delocalizations between aromatic systems were observed, particularly in complex **2a**, where the π(N6–C26) → π*(N7–C9) interaction shows a substantial stabilization energy of 85.94 kcal/mol. This suggests an extensive conjugation network and effective electron delocalization within the ligand framework. Complexes **2b–e** display similar but comparatively lower π-delocalization energies (around 20–30 kcal/mol), reflecting subtle variations in electronic communication influenced by substituent patterns. Lone pairs on the palladium center (LP) also contribute to metal-to-ligand back-donation, as evidenced by LP(Pd1) → π*(N7–C9) interactions ranging between 9.64 and 14.87 kcal/mol. These interactions highlight the role of Pd in donating electron density back into ligand antibonding orbitals, thereby enhancing complex stability. Throughout all complexes, the lone pairs on N8 nitrogen atoms (LP (1) N8) strongly stabilize the Pd–carbene bond, with donor–acceptor interaction energies ranging from 17.45 to 21.27 kcal/mol. In summary, the NBO analysis demonstrates that the Pd (II) complexes possess strong and multifaceted metal-ligand bonding, alongside significant ligand-ligand electronic communication. These factors collectively contribute to the complexes' stability and reactivity profiles.

3.7 The Pd-PEPPSI complexes catalyzed Suzuki reaction

The Suzuki reaction is of great importance in modern organic synthesis due to its advantages such as high efficiency in the formation of carbon-carbon bonds, a wide range of substrates, and mild reaction conditions. This reaction is widely used in the synthesis of biologically active molecules, pharmaceutical compounds, and advanced functional materials. To evaluate the catalytic activities of complexes **2a-e**, various aryl chlorides were coupled with phenylboronic acid, as summarized in Table 6. Initially, 4-chloroacetophenone was selected as a model substrate for the optimization of reaction conditions. A yield of 32% was obtained using K_2CO_3 as the base in an *i*-PrOH: water solvent system (Table 6, entry 3). In contrast, employing dimethylformamide (DMF): water as the solvent under otherwise identical conditions significantly improved the yield to 61% (Table 6, entry 4). Notably, when the reaction was conducted in *i*-PrOH: water using optimized conditions, the yield increased to 84% (Table 6, entry 5). For comparison, the use of palladium(II) acetate ($Pd(OAc)_2$) and $PdCl_2$ as palladium sources afforded yields of 53% and 62%, respectively (Table 6, entries 1 and 2). The results reveal that the catalytic efficiency strongly depends on both the nature of the NHC ligand and the electronic properties of the aryl chloride substituent. In the case of aryl chlorides bearing electron-withdrawing substituents such as $COCH_3$ and CHO, enhanced catalytic activity was observed for all Pd–PEPPSI complexes compared to simple Pd precursors ($Pd(OAc)_2$ and $PdCl_2$). Electron-deficient aryl chlorides are known to facilitate the oxidative addition step by increasing the polarization of the C–Cl bond, thereby lowering the activation barrier for Pd(0) insertion. Consequently, complexes **2e**, **2a**, and **2c** exhibited superior performance, affording yields of up to 79% for 4-chloroacetophenone. The presence of strongly σ-donating NHC ligands in these complexes further stabilizes the Pd center and promotes efficient oxidative addition. For the unsubstituted aryl chloride (R = H), uniformly high yields (> 79%) were obtained with all Pd–PEPPSI complexes, indicating that these catalysts are well suited to activate relatively unactivated C–Cl bonds. Among them, complex **2e** delivered the highest yield (88%), followed by **2b** (86%) and **2d** (83%). This enhanced reactivity can be attributed to the optimal balance between steric bulk and electron donation provided by the NHC ligand in **2e**, which facilitates oxidative addition while minimizing catalyst deactivation pathways such as aggregation or formation of inactive Pd species. In contrast, aryl chlorides bearing an electron-donating CH_3 substituent exhibited significantly lower reactivity under identical conditions. Electron-rich substrates reduce the electrophilicity of the aryl carbon and strengthen the C–Cl bond, thereby disfavoring oxidative addition and leading to decreased catalytic efficiency. Although all catalysts were affected by this electronic factor, complex **2e** again showed the best performance (78% yield), suggesting that its ligand environment is particularly effective in compensating for the reduced intrinsic reactivity of electron-rich aryl chlorides. The lower yields observed with the other complexes highlight the sensitivity of the catalytic system to subtle variations in NHC ligand sterics and electronics. Overall, the results highlight that Pd–PEPPSI complexes outperform simple Pd salts in the Suzuki–Miyaura reaction. Among the tested catalysts, complex **2e** emerged as the most versatile and efficient overall, especially for electron-neutral and electron-deficient aryl chlorides. These findings underscore the importance of fine-tuning NHC ligand sterics and electronics to optimize catalyst performance for different substrate classes. The results once again demonstrate that the Suzuki reaction is an effective method in terms of both structural diversity and efficiency.

Table 6 Suzuki reaction catalyzed by Pd-PEPPSI complexes



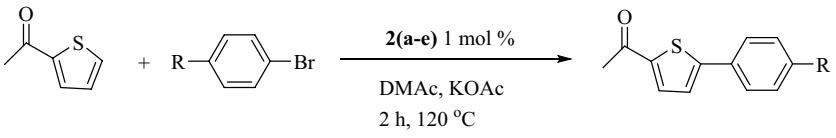
Entry	R	Time (h)	Catalyst	Yield (%)	
				1	2
1	$COCH_3$	5	$Pd(OAc)_2$	21	32
2	$COCH_3$	5	$PdCl_2$	17	45
3	$COCH_3$	3	**2b**	12	20[a]
4	$COCH_3$	3	**2b**	13	48[b]
5	$COCH_3$	3	**2a**	8	76
6	$COCH_3$	3	**2b**	6	71
7	$COCH_3$	3	**2c**	14	75
8	$COCH_3$	3	**2d**	13	65
9	$COCH_3$	3	**2e**	9	81
10	COH	3	**2a**	11	67
11	COH	3	**2b**	8	65
12	COH	3	**2c**	14	67
13	COH	3	**2d**	5	71
14	COH	3	**2e**	11	79
15	H	3	**2a**	-	79
16	H	3	**2b**	-	86
17	H	3	**2c**	-	81
18	H	3	**2d**	-	83
19	H	3	**2e**	-	88
20	CH_3	3	**2a**	31	25
21	CH_3	3	**2b**	26	17
22	CH_3	3	**2c**	50	23
23	CH_3	3	**2d**	41	27
24	CH_3	3	**2e**	48	30

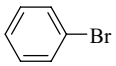
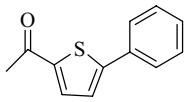
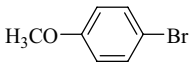
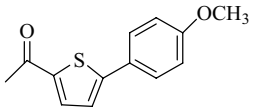
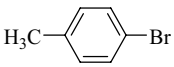
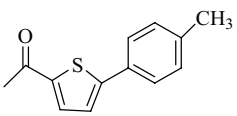
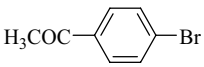
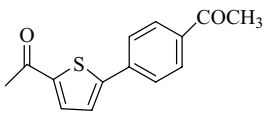
Conditions: Phenyl boronic acid (1.2 mmol), aryl chloride (1.0 mmol), Pd catalyst (0.25 mol%), Cs_2CO_3 (1.0 mmol), *i*-PrOH: Water (1:3), 55 °C, 3 h. Product purity was checked by GC, yields were calculated according to aryl chloride. a: K_2CO_3 was used as the base, b: K_2CO_3 was used as the base and DMF: H_2O was used as the solvent

3.8 The Pd-PEPPSI complexes catalyzed direct arylation of 2-acetylthiophene with aryl bromides

The catalytic activity of the prepared **2a-e** complexes in the arylation of 2-acetylthiophene with aryl bromides was investigated under optimized conditions (DMAc, KOAc, 120 °C, 2 h). As demonstrated in Table 7, the reaction proceeded in a highly efficient manner in the presence of all of the substrates that were tested. The corresponding arylated products were obtained in moderate to excellent yields. The

Table 7 Pd-PEPPSI complexes catalyzed direct arylation of 2-acetylthiophene with aryl bromides



Entry	Aryl bromide	Product	(1a-e)	Yield (%)
1			2a	62
2			2b	73
3			2c	69
4			2d	68
5			2e	77
6			2a	47
7			2b	51
8			2c	59
9			2d	63
10			2e	65
11			2a	83
12			2b	84
13			2c	79
14			2d	81
15			2e	86
16			2a	94
17			2b	98
18			2c	96
19			2d	98
20			2e	98
21			-	0
22			$PdCl_2$	54[a]

Conditions: 2-acetyl thiophene (2.0 mmol), aryl bromide (1.0 mmol), 2a-e (1 mol %), KOAc (1.0 mmol), N,N-dimethylacetamide (2 ml), 120 °C, 2 h. Product purity was checked by GC and, yields were calculated according to aryl bromide, a: the reaction was completed in 8 h

variation in product yields can be rationalized by considering the electronic nature of the aryl bromides and their influence on the key steps of the catalytic cycle, particularly oxidative addition and subsequent C–H activation. For unsubstituted aryl bromides (Entries 1–5), yields in the range of 62–77% were obtained, demonstrating that **2a-e** complexes can efficiently support the coupling process under optimized conditions. These results indicate that the Pd–PEPPSI framework provides a sufficiently active Pd(0) species capable of activating relatively neutral C–Br bonds. However, the absence of strong electronic bias in these substrates results in only moderate facilitation of oxidative addition, which likely limits the overall reaction rate and product yield under the applied conditions. Substrates containing weak electron-donating groups such as methoxy (Entries 6–10) provided only moderate yields (47–65%). This decrease in efficiency can be attributed to the strong resonance donation of the methoxy group, which increases electron density on the aryl carbon bonded to bromine and consequently diminishes the electrophilicity of the C–Br bond. As a result, oxidative addition to the Pd center becomes less favorable. In contrast, aryl bromides containing stronger electron-donating substituents such as methyl groups (Entries 11–15) provided significantly higher yields (79–86%). This observation can be

explained by the increased electron density on the aryl ring, which facilitates the oxidative addition step of the catalytic cycle. The best results were obtained using 4-bromoacetophenone (Entries 16–20), where the desired products were isolated in excellent yields (94–98%). The presence of a strongly electron-withdrawing carbonyl group significantly enhances polarization of the C–Br bond, thereby lowering the activation barrier for oxidative addition. Moreover, the carbonyl functionality may stabilize key catalytic intermediates through secondary interactions, further promoting efficient C–H activation and reductive elimination steps. The reaction was also tested without any palladium source and using $PdCl_2$ as the palladium source (Entries 21,22). While no product yield was observed for the blank test after 8 h of reaction, a product yield of 54% was obtained in the presence of $PdCl_2$. These findings demonstrate that the Pd-PEPPSI system exhibits particularly high catalytic efficiency when applied to electron-rich aryl halides.

4 Conclusion

In this study, five new NHC-based Pd-PEPPSI complexes (**2a–e**) were successfully designed, synthesized, and characterized by experimental and computational methods. The catalytic activities of the prepared complexes in the Suzuki reaction and the arylation of 2-acetylthiophene were investigated. The obtained results demonstrated the efficacy of the catalysts in both catalytic applications, with complex **2e** exhibiting the highest activity. In addition, the integration of spectroscopic analysis, X-ray crystallography, and DFT calculations validated their structural integrity, thereby facilitating a comprehensive comprehension of their bonding and electronic properties. The HOMO distributions indicate that the Pd center and bromide ligands are the primary sites for electron transfer during catalysis. The comparable HOMO–LUMO gaps of complexes **2a–e** point to similar intrinsic reactivity, while the higher stability and polarizability of complex **2e** suggest improved electronic–structural balance under catalytic conditions. In addition, NBO analysis reveals significant metal–ligand donor–acceptor interactions, particularly involving σ(Pd–C) → σ*(Pd–Br) and LP(Pd) → π*(ligand) transitions, which reflect efficient back-donation and electronic delocalization within the coordination sphere. These interactions stabilize key catalytic intermediates and reduce the likelihood of catalyst deactivation pathways such as aggregation or ligand dissociation. Collectively, these structural and orbital-level features explain why complex **2e** exhibits superior catalytic performance, as its ligand environment provides both strong electronic activation of the Pd center and sufficient steric protection to sustain the catalytic cycle efficiently.

Supplementary Information The online version contains supplementary material available at https://doi.org/10.1007/s11244-026-02281-6.

Acknowledgements The numerical calculations reported in this paper were partially performed at TUBITAK ULAKBIM, High Performance and Grid Computing Center (TRUBA resources).

Funding Open access funding provided by the Scientific and Technological Research Council of Türkiye (TÜBİTAK).

Declarations

Conflict of interest There are no conflicts to declare.

Open Access This article is licensed under a Creative Commons Attribution 4.0 International License, which permits use, sharing, adaptation, distribution and reproduction in any medium or format, as long as you give appropriate credit to the original author(s) and the source, provide a link to the Creative Commons licence, and indicate if changes were made. The images or other third party material in this article are included in the article's Creative Commons licence, unless indicated otherwise in a credit line to the material. If material is not included in the article's Creative Commons licence and your intended use is not permitted by statutory regulation or exceeds the permitted use, you will need to obtain permission directly from the copyright holder. To view a copy of this licence, visit http://creativecommons.org/licenses/by/4.0/.

References

1. Rahman M, Zhang J, Zhao Q, Feliciano J et al (2022) Pd–PEPPSI N-heterocyclic carbene complexes from caffeine: applicationin Suzuki, Heck, and Sonogashira reactions. Organometallics 41:2281 – 2290. https://doi.org/10.1021/acs.organomet.2c00262
2. Albano G, Punzi A, Farinola GM (2022) Sustainable protocols for direct C–H bond arylation of (hetero)arenes. Green Chem 24:1809–1894. https://doi.org/10.1039/d1gc03168f
3. Gogoi B, Khargharia S, Kar R et al (2024) A new air-stable Pd-PEPPSI N-heterocyclic carbene complex: Synthesis, structure, computational and catalytical studies. J Mol Struct 295:136678. https://doi.org/10.1016/j.molstruc.2023.136678
4. Sandeli AE, Boulebda H, Khiri-Meribout N et al (2022) New benzimidazolium *N*-heterocyclic carbene precursors and their related Pd-NHC complex PEPPSI-type: Synthesis, structures, DFT calculations, biological activity, docking study, and catalytic application in the direct arylation. J Mol Struct 1248:131504. https://doi.org/10.1016/j.molstruc.2021.131504
5. Zhu L, Gao T, Shao L (2011) Well-defined NHC-Pd(II)-Im (NHC = N-heterocyclic carbene; Im = 1-methylimidazole) complexes catalyzed amination of aryl chlorides. Tetrahedron 67:5150–5155. https://doi.org/10.1016/j.tet.2011.05.057
6. Soni A, Sharma C, Negi L et al (2023) NHC-Pd(II) full pincer catalyzed Mizoroki-Heck type cross-coupling of vinyl chloride and alkenes: synthesis of novel ferrocenylated conjugated dienes. J Organomet Chem 983:122550. https://doi.org/10.1016/j.jorganchem.2022.122550
7. Yang L, Li Y, Chen Q et al (2013) Sonogashira/hydroarylation sequential reactions: catalyzed by NHC-Pd complexes. Tetrahedron 69:5178–5184. https://doi.org/10.1016/j.tet.2013.04.061
8. Vasu GRP, Venkata KRM, Kakarla RR et al (2023) Recent advances in sustainable N-heterocyclic carbene-Pd(II)-pyridine

(PEPPSI) catalysts: A review. Environ Res 225:115515. https://doi.org/10.1016/j.envres.2023.115515
9. Mazars F, Zaragoza G, Delaude L (2022) Caffeine and theophylline as sustainable, biosourced NHC ligand precursors for efficient palladium-catalyzed Suzuki–Miyaura cross-coupling reactions. J Organomet Chem 978:122489. https://doi.org/10.1016/j.jorganchem.2022.122489
10. Aravinda RP, Babul RA, Ramachandra RG, Subbarami RN (2013) Suzuki–miyaura cross-coupling reaction of naphthyl triflate with ındole boronic acids catalyzed by a recyclable polymer-supported N-heterocyclic carbene–palladium complex catalyst: synthesis of naphthalene-linked bis-heterocycles. J Heterocycl Chem 50:14511456. https://doi.org/10.1002/jhet.1090
11. Marzano G, Carulli F, Babudri F et al (2016) PBDTTPD for plastic solar cells via $Pd(PPh_3)_4$-catalyzed direct (hetero)arylation polymerization. J Mater Chem A 4:17163–17170. https://doi.org/10.1039/C6TA06679H
12. Mata JA, Poyatos M, Peris E (2007) Structural and catalytic properties of chelating bis- and tris-N-heterocyclic carbenes. Coord Chem Rev 251:841–859. https://doi.org/10.1016/j.ccr.2006.06.008
13. Shi S, Nolan SP, Szostak M (2018) Well-defined Palladium(II)–NHC precatalysts for cross-coupling reactionsof amides and esters by selective N–C/O–C cleavage. Acc Chem Res 51(10):2589–2599. https://doi.org/10.1021/acs.accounts.8b00410
14. Ackermann L, Vincente R, Kapdi AR (2009) Transition-metal-catalyzed direct arylation of (hetero)arenes by C-H bond cleavage. Angew Chem Int Ed 48:9792–9826. https://doi.org/10.1002/anie.200902996
15. Zhao Q, Meng G, Nolan SP, Szostak M (2020) N-heterocyclic carbene complexes in C–H activation reactions. Chem Rev 120(4):1981–2048. https://doi.org/10.1021/acs.chemrev.9b00634
16. Roger J, Gottumukkala AL, Doucet H (2010) regiocontroled palladium-catalysed direct arylation at carbon C2 of benzofurans using benzenesulfonyl chlorides as the coupling partners. Chem Cat Chem 2:20–40. https://doi.org/10.1002/cctc.201301077
17. O'Brien CJ, Kantchev EAB, Valente C et al (2006) Easily prepared air- and moisture-stable Pd–NHC (NHC=N-heterocyclic carbene) complexes: a reliable, user-friendly, highly active palladium precatalyst for the Suzuki–Miyaura reaction. Chem Eur J 12:4743–4748. https://doi.org/10.1002/CHEM.200600251
18. Kurpik G, Walczak A, Gołdyn M et al (2022) Pd(II) Complexes with pyridine ligands: substituent effects on the nmr data, crystal structures, and catalytic activity. Inorg Chem 61:14019–14029. https://doi.org/10.1021/acs.inorgchem.2c01996
19. Muniyappan N, Budagumpi S (2026) Recent advances in PEPPSI–themed palladium NHC complexes: Applications ranging from homogeneous catalysis to electrocatalysis. Inorg Chim Acta 589:122915. https://doi.org/10.1016/j.ica.2025.122915
20. Kader DA, Sidiq MK, Taher SG, Aziz DM (2025) Recent advances in palladium-catalyzed Suzuki-Miyaura cross-coupling reactions: Exploration of catalytic systems, reaction parameters, and ligandinfluences: A review. J Organomet Chem 1030:123569. https://doi.org/10.1016/j.jorganchem.2025.123569
21. Bruker (2013) APEX2 and SAINT. Bruker AXS Inc., Madison, Wisconsin, USA
22. Sheldrick GM (2015) SHELXT – Integrated space-group and crystal-structure determination. Acta Cryst A 71:3–8. https://doi.org/10.1107/S2053273314026370
23. Sheldrick GM (2015) Crystal structure refinement with SHELXL. Acta Cryst C 71:3–8. https://doi.org/10.1107/S2053229614024218
24. Dolomanov OV, Bourhis LJ, Gildea RJ et al (2009) OLEX2: a complete structure solution, refinement and analysis program. J Appl Cryst 42:339–341. https://doi.org/10.1107/S0021889808042726
25. Frisch MJ, Trucks GW, Schlegel HB, Scuseria GE (2016) Gaussian 16 Rev. C.01. Wallingford. CT
26. Becke AD (1993) A new mixing of Hartree-Fock and local density-functional theories. J Chem Phys 98:1372. https://doi.org/10.1063/1.464304
27. Lee C, Yang W, Parr RG (1988) Development of the Colle-Salvetti correlation-energy formula into a functional of the electron density. Phys Rev B 37:785. https://doi.org/10.1103/PhysRevB.37.785
28. Becke AD (1993) Density-functional thermochemistry. III. The role of exact Exchange. J Chem Phys 98:5648–5652. https://doi.org/10.1063/1.464913
29. Hay PJ, Wadt WR (1985) Ab initio efective core potentials for molecular calculations. Potentials for K to Au including the outermost core orbitals. J Chem Phys 82:299–310. https://doi.org/10.1063/1.44897.5
30. Dennington R, Keith TA, Millam JM (2016) GaussView. Version 6 Semichem Inc. Shawnee Mission. KS
31. Rahman S, Hussain A, Noreen S et al (2023) Structural, electronic, optical and mechanical properties of oxide-based perovskite ABO3 (A=Cu, Nd and B=Sn, Sc): A DFT study. J Solid State Chem 317:123650. https://doi.org/10.1016/j.jssc.2022.123650
32. McQuarrie DA (1973) Statistical thermodynamics. Harper & Row, New York
33. Hill TL (1962) An introduction to statistical thermodynamics. Addison- Wesley Publishing, Inc, London
34. Herzberg G (1964) Molecular Spectra and Molecular Structure III, 1. Edition, D. Van Nostrand Company, Inc., New York
35. Serdaroğlu G, Durmaz S (2010) DFT and statistical mechanics entropy calculations of diatomic and polyatomic molecules. Indian J Chem 49:861–866
36. Koopmans T (1934) Über die zuordnung von wellenfunktionen und eigenwerten zu den einzelnen elektronen eines atoms. Physica 1–6:104–113. https://doi.org/10.1016/S0031-8914(34)90011-2
37. Parr RG (1999) Electrophilicity index. J Am Chem Soc 121:1922. https://doi.org/10.1021/ja983494x
38. Parr RG, Pearson RG (1983) Absolute hardness: companion parameter to absolute electronegativity. J Am Chem Soc 105:7512–7516
39. Pearson RG (1986) Absolute electronegativity and hardness correlated with molecular orbital theory. Proc Natl Acad Sci U S A 83:8440. https://doi.org/10.1073/pnas.83.22.8440
40. Perdew JP, Levy M (1983) Physical content of the exact kohn-sham orbital energies: band gaps and derivative discontinuities. Phys Rev Let 51:1884. https://doi.org/10.1103/PhysRevLett.51.1884
41. Perdew JP, Parr RG, Levy M, Balduz JL (1982) Density-functional theory for fractional particle number: derivative discontinuities of the energy. Phys Rev Let 49:1691. https://doi.org/10.1103/PhysRevLett.49.1691
42. Gazquez JL, Cedillo A, Vela A (2007) Electrodonating and electroaccepting powers. J Phys Chem A 111(10):1966–1970. https://doi.org/10.1021/jp065459f
43. Gomez B, Likhanova NV, Domínguez-Aguilar MA et al (2006) Quantum chemical study of the inhibitive properties of 2-pyridylazoles. J Phys Chem B 110(18):8928–8934. https://doi.org/10.1021/jp057143y
44. Weinhold, Landis CR, Glendening ED (2016) What is NBO analysis and how is it useful? Int Rev Phys Chem 35:399–440. https://doi.org/10.1080/0144235X.2016.1192262
45. Reed AE, Curtiss LA, Weinhold F (1988) Intermolecular interactions from a natural bond orbital, donor-acceptor viewpoint. Chem Rev 88(6):899–926
46. Ozdemir I, Gök Y, Ozeroğlu O et al (2010) N-heterocyclic carbenes: Useful ligands for the Palladium-catalysed direct C5

arylation of heteroaromatics with aryl bromides or electron-deficient aryl chlorides. Eur J Inorg Chem 12:1798. https://doi.org/10.1002/ejic.200901195
47. Yang L, Powell DR, Houser RP (2007) Structural variation in copper(i) complexes with pyridylmethylamide ligands: structural analysis with a new four-coordinate geometry index, τ_4. Dalton Trans 9:955–964. https://doi.org/10.1039/B617136B
48. Okuniewski A, Rosiak D, Chojnacki J, Becker B (2015) Coordination polymers and molecular structures among complexes of mercury(II) halides with selected 1-benzoylthioureas. Polyhedron 90:47–57. https://doi.org/10.1016/j.poly.2015.01.035
49. Reineke MH, Sampson MD, Rheingold AL, Kubiak CP (2015) Synthesis and structural studies of nickel(0) tetracarbene complexes with the introduction of a new four-coordinate geometric index, τ_δ. Inorg Chem 54:3211–3217. https://doi.org/10.1021/ic502792q
50. Cordero B, Gomez V, Platero-Prats AE et al (2008) Covalent radii revisited. Dalton Trans 21:2832–2838. https://doi.org/10.1039/B801115J
51. Doğan Ulu Ö, Serin S, Özdemir N, Özdemir İ (2025) Synthesis, crystal structure, and DFT studies of NHC mediated Pd-PEPPSI complex: Application for Suzuki reaction. J Mol Struct 1320:139479. https://doi.org/10.1016/j.molstruc.2024.139479
52. Kaloğlu M, Özdemir İ, Dorcet V et al (2017) PEPPSI-type palladium–NHC complexes: synthesis, characterization, and catalytic activity in the direct C5-arylation of 2-substituted thiophene derivatives with aryl halides. Eur J Inorg Chem 10:1382–1391. https://doi.org/10.1002/ejic.201601452
53. Kaloğlu N, Kaloğlu M, Tahir MN et al (2018) Synthesis of N-heterocyclic carbene-palladium-PEPPSI complexes and their catalytic activity in the direct C-H bond activation. J Organomet Chem 867:404–412. https://doi.org/10.1016/j.jorganchem.2017.10.019
54. Han Y, Huynh HV, Tan GK (2007) Syntheses and characterizations of Pd(II) complexes incorporating a N-heterocyclic carbene and aromatic N-heterocycles. Organometallics 26:6447–6452. https://doi.org/10.1021/om700753d
55. Huynh HV, Sim W, Chin CF (2011) Rotaxanes with Palladium(II)-NHC stoppers. Dalton Trans. https://doi.org/10.1039/C1DT11472G. 40:11690 – 11692
56. Lin YC, Hsueh HH, Kanne S et al (2013) Efficient PEPPSI-themed palladium N-heterocyclic carbene precatalysts for the Mizoroki–Heck reaction. Organometallics 32:3859–3869. https://doi.org/10.1021/om4003297
57. Barbu L, Popa MM, Shova S et al (2017) New Pd-NHC PEPPSI complexes from benzimidazolium salts with a phenacyl group attached to N_3. Inorg Chim Acta 463:97–101. https://doi.org/10.1016/j.ica.2017.04.024
58. Kaloğlu M, Kaloğlu N, Yıldırım İ et al (2020) Palladium-carbene catalyzed direct arylation of five-membered heteroaromatics. J Mol Struct 1206:127668. https://doi.org/10.1016/j.molstruc.2019.127668
59. Sandeli A, Khiri-Meribout N, Benzerka S (2021) Synthesis, structures, DFT calculations, and catalytic application in the direct arylation of five-membered heteroarenes with aryl bromides of novel palladium-N-heterocyclic carbene PEPPSI-type complexes. New J Chem 45:17878–17892. https://doi.org/10.1039/D1NJ03388C
60. Cremer D, Pople JA (1975) General definition of ring puckering coordinates. J Am Chem Soc 97. https://doi.org/10.1021/ja00839a011. :1354 – 1358
61. Sundaraganesan N, Ilakiamani S, Salem H et al (2005) Spectrochimica Acta Part A: Mol Biomol Spectrosc 61:2995–3001
62. Krishnakumar V, Xavier RJ (2004) Vibrational spectra and assignments of benzimidazole. Spectrochim Acta A 60:709–715
63. Yamada S, Ichikawa M (1979) Infrared studies of pyridine adsorption and ring vibrations. J Mol Struct 57:1–12
64. Lin-Vien D, Colthup NB, Fateley WG, Grasselli JG (1991) The Handbook of Infrared and Raman. Characteristic Frequencies of Organic Molecules; Academic
65. Murray JS, Politzer P (2011) The electrostatic potential: an overview. Wiley Interdiscip Rev Comput Mol Sci 1:153–163. https://doi.org/10.1002/wcms.19
66. Murray JS, Sen K (1996) Molecular electrostatic potentials: concepts and applications, first edn. Elsevier, Amsterdam

Publisher's Note Springer Nature remains neutral with regard to jurisdictional claims in published maps and institutional affiliations.